



Plasma Plume Characterization of the HERMeS During a 1722-hr Wear Test Campaign

Wensheng Huang and George J. Williams
Glenn Research Center, Cleveland, Ohio

Peter Y. Peterson
Vantage Partners, LLC, Brook Park, Ohio

Hani Kamhawi
Glenn Research Center, Cleveland, Ohio

James H. Gilland
Ohio Aerospace Institute, Brook Park, Ohio

Daniel A. Herman
Glenn Research Center, Cleveland, Ohio

Prepared for the
35th International Electric Propulsion Conference
sponsored by IEPC
Atlanta, Georgia, October 8–12, 2017

NASA STI Program . . . in Profile

Since its founding, NASA has been dedicated to the advancement of aeronautics and space science. The NASA Scientific and Technical Information (STI) Program plays a key part in helping NASA maintain this important role.

The NASA STI Program operates under the auspices of the Agency Chief Information Officer. It collects, organizes, provides for archiving, and disseminates NASA's STI. The NASA STI Program provides access to the NASA Technical Report Server—Registered (NTRS Reg) and NASA Technical Report Server—Public (NTRS) thus providing one of the largest collections of aeronautical and space science STI in the world. Results are published in both non-NASA channels and by NASA in the NASA STI Report Series, which includes the following report types:

- **TECHNICAL PUBLICATION.** Reports of completed research or a major significant phase of research that present the results of NASA programs and include extensive data or theoretical analysis. Includes compilations of significant scientific and technical data and information deemed to be of continuing reference value. NASA counter-part of peer-reviewed formal professional papers, but has less stringent limitations on manuscript length and extent of graphic presentations.
- **TECHNICAL MEMORANDUM.** Scientific and technical findings that are preliminary or of specialized interest, e.g., "quick-release" reports, working papers, and bibliographies that contain minimal annotation. Does not contain extensive analysis.
- **CONTRACTOR REPORT.** Scientific and technical findings by NASA-sponsored contractors and grantees.
- **CONFERENCE PUBLICATION.** Collected papers from scientific and technical conferences, symposia, seminars, or other meetings sponsored or co-sponsored by NASA.
- **SPECIAL PUBLICATION.** Scientific, technical, or historical information from NASA programs, projects, and missions, often concerned with subjects having substantial public interest.
- **TECHNICAL TRANSLATION.** English-language translations of foreign scientific and technical material pertinent to NASA's mission.

For more information about the NASA STI program, see the following:

- Access the NASA STI program home page at <http://www.sti.nasa.gov>
- E-mail your question to help@sti.nasa.gov
- Fax your question to the NASA STI Information Desk at 757-864-6500
- Telephone the NASA STI Information Desk at 757-864-9658
- Write to:
NASA STI Program
Mail Stop 148
NASA Langley Research Center
Hampton, VA 23681-2199



Plasma Plume Characterization of the HERMeS During a 1722-hr Wear Test Campaign

Wensheng Huang and George J. Williams
Glenn Research Center, Cleveland, Ohio

Peter Y. Peterson
Vantage Partners, LLC, Brook Park, Ohio

Hani Kamhawi
Glenn Research Center, Cleveland, Ohio

James H. Gilland
Ohio Aerospace Institute, Brook Park, Ohio

Daniel A. Herman
Glenn Research Center, Cleveland, Ohio

National Aeronautics and
Space Administration

Glenn Research Center
Cleveland, Ohio 44135

Acknowledgments

The authors would like to thank the Space Technology Mission Directorate through the Solar Electric Propulsion Technology Demonstration Mission Project for funding the joint NASA Glenn Research Center (GRC) and Jet Propulsion Laboratory (JPL) development of the HERMeS thruster and this work. The authors would like to thank Todd Tofil for managing the electric propulsion work within the SEP Project and the thruster lead, Richard R. Hofer, for managing the thruster work. The authors would also like to thank Christopher M. Griffiths, John T. Yim, Thomas W. Haag, Timothy R. Sarver-Verhey, Jonathan A. Mackey, Lauren K. Clayman, James L. Myers, Li C. Chang, Dale A. Robinson, Maria Choi, Timothy Gray, Jason Frieman of the NASA Glenn Research Center and James E. Polk, Ioannis G. Mikellides, Alejandro Lopez Ortega, Benjamin A. Jorns, Michael J. Sekerak, Ryan W. Conversano, Vernon H. Chaplin of the Jet Propulsion Laboratory for work on the SEP TDM HERMeS Hall thruster. And the authors would like to thank Michael W. Swiatek, Richard G. Senyitko, Kevin L. Blake, George P. Jacynycz, Thomas A. Ralys, and Terrell J. Jensen for assembly of the test setup, and operation of the vacuum facility.

Trade names and trademarks are used in this report for identification only. Their usage does not constitute an official endorsement, either expressed or implied, by the National Aeronautics and Space Administration.

Level of Review: This material has been technically reviewed by technical management.

Available from

NASA STI Program
Mail Stop 148
NASA Langley Research Center
Hampton, VA 23681-2199

National Technical Information Service
5285 Port Royal Road
Springfield, VA 22161
703-605-6000

This report is available in electronic form at <http://www.sti.nasa.gov/> and <http://ntrs.nasa.gov/>

Plasma Plume Characterization of the HERMeS During a 1722-hr Wear Test Campaign

Wensheng Huang and George J. Williams
National Aeronautics and Space Administration
Glenn Research Center
Cleveland, Ohio 44135

Peter Y. Peterson
Vantage Partners, LLC
Brook Park, Ohio 44142

Hani Kamhawi
National Aeronautics and Space Administration
Glenn Research Center
Cleveland, Ohio 44135

James H. Gilland
Ohio Aerospace Institute
Brook Park, Ohio 44142

Daniel A. Herman
National Aeronautics and Space Administration
Glenn Research Center
Cleveland, Ohio 44135

Abstract

A 1722-hr wear test campaign of NASA's 12.5-kW Hall Effect Rocket with Magnetic Shielding was completed. This wear test campaign, completed in 2016, was divided into four segments including an electrical configuration characterization test, two short duration tests, and one long wear test. During the electrical configuration characterization test, the plasma plume was examined to provide data to support the down select of the electrical configuration for further testing. During the long wear tests, the plasma plume was periodically examined for indications of changes in thruster behavior. Examination of the plasma plume data from the electrical configuration characterization test revealed a correlation between the plume properties and the presence of a conduction path through the front poles. Examination of the long wear test plasma plume data revealed that the plume characteristics remained unchanged during testing to within the measurement uncertainty.

Nomenclature

AEPS	Advanced Electric Propulsion System
CEX	Charge-exchange
ECCT	Electrical Configuration Characterization Test
FP	Faraday Probe
GRC	Glenn Research Center
HERMeS	Hall Effect Rocket with Magnetic Shielding
IPS	Ion Propulsion System
JPL	Jet Propulsion Laboratory

LP	Langmuir Probe
MCD	Mean Channel Diameter
RFC	Reference Firing Condition
RPA	Retarding Potential Analyzer
SEE	Secondary Electron Emission
SEP	Solar Electric Propulsion
STMD	Space Technology Mission Directorate
TDM	Technology Demonstration Mission
TDU	Technology Demonstration Unit
VF	Vacuum Facility
WFS	Wien Filter Spectrometer
WT	Wear Test

1.0 Introduction

For missions beyond low Earth orbit, spacecraft size and mass can be dominated by onboard chemical propulsion systems and propellants that may constitute more than 50 percent of spacecraft mass. This impact can be substantially reduced through the utilization of Solar Electric Propulsion (SEP) due to its substantially higher specific impulse. Studies performed for NASA's Human Exploration and Operations Mission Directorate (HEOMD) and Science Mission Directorate have demonstrated that a 40 kW-class SEP capability can be enabling for both near term and future architectures and science missions (Ref. 1).

Since 2012 NASA has been developing a 14-kW Hall thruster electric propulsion string that can serve as the building block for realizing a 40-kW-class SEP capability. NASA continues to evolve a human exploration approach to expand human presence beyond low Earth orbit and to do so, where practical, in a manner involving international, academic, and industry partners (Ref. 2). NASA publicly presented a phased exploration concept at the HEOMD Committee of the NASA Advisory Council meeting on March 28, 2017 (Ref. 3). NASA presented an evolutionary human exploration architecture, depicted in Figure 1, to expand human presence deeper into the solar system through a phased approach including cis-lunar flight testing and validation of exploration capability before crewed missions beyond the

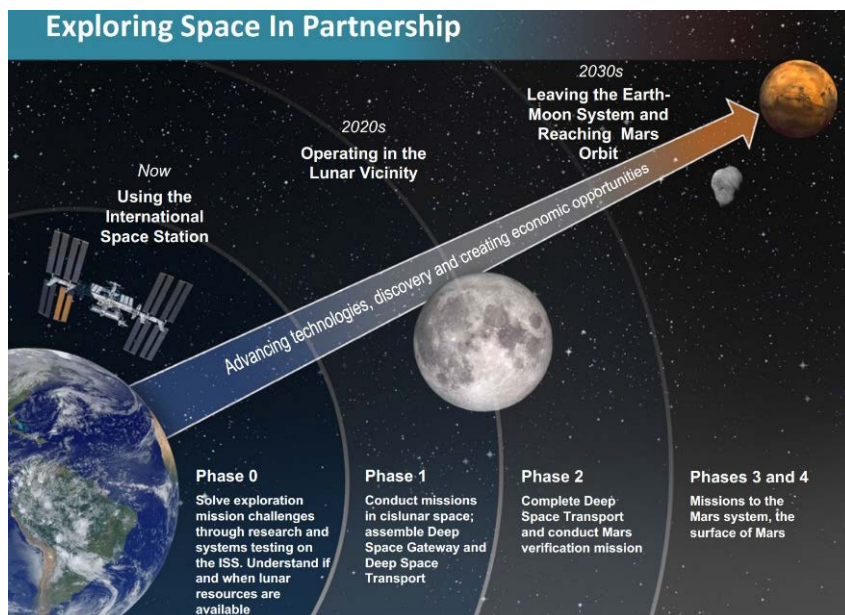


Figure 1.—Deep space gateway and transport plan depiction (Ref. 5).

Earth-Moon system and eventual crewed Mars missions. One of the key objectives is to achieve human exploration of Mars and beyond through the prioritization of those technologies and capabilities best suited for such a mission in accordance with the stepping stone approach to exploration (Ref. 4).

High-power solar electric propulsion is one of those key technologies that has been prioritized because of its significant exploration benefits. A high-power, 40 kW-class Hall thruster propulsion system provides significant capability and represents, along with flexible blanket solar array technology, a readily scalable technology with a clear path to much higher power systems.

The 14-kW Hall thruster system development, led by the NASA Glenn Research Center (GRC) and the Jet Propulsion Laboratory (JPL), began with maturation of the high-power Hall thruster and power processing unit. The technology development work has transitioned to Aerojet Rocketdyne via a competitive procurement selection for the Advanced Electric Propulsion System (AEPS). The AEPS contract includes the development, qualification, and multiple flight 14-kW electric propulsion string deliveries. The AEPS Electric Propulsion string consists of the Hall thruster, power processing unit (including digital control and interface functionality), xenon flow controller, and associated intra-string harnesses. These components are also collectively known as the Ion Propulsion System (IPS). NASA continues to support the AEPS development leveraging in-house expertise, plasma modeling capability, and world-class test facilities. NASA also executes AEPS and mission risk reduction activities to support the AEPS development and mission application.

Risk reduction activities are being carried out on the precursor to AEPS known as the Hall Effect Rocket with Magnetic Shielding (HERMeS) (Refs. 6 and 7). The specifications for the 12.5-kW HERMeS are enhanced compared to the current state of the art (Ref. 6). Characteristics of the thruster include high system efficiency (≥ 57 percent), high specific impulse (up to 3000 s), and high propellant throughput capability (3400 kg). Additionally, HERMeS was designed to deliver similar system efficiency at a more modest specific impulse of 2000 s. High specific impulse operation supports mission concepts with high total-impulse requirements like deep-space exploration missions, while the modest specific impulse operation is beneficial for time-critical operations like LEO to GEO orbit raising.

A series of tests are being performed on three HERMeS Technology Development Units (TDUs) (Ref. 7). Figure 2 shows a diagram of the testing on the HERMeS TDUs thus far as well as tests that are planned. Testing on the TDU1 included the propellant uniformity test (Ref. 8), magnetic shielding characterization test (Ref. 9), performance characterization test (PCT) (Refs. 10 to 12), thermal characterization test (TCT) (Refs. 13 and 14), facility effect characterization test (FECT) (Refs. 10, 12, and 15), and the first wear test (WT) campaign. The PCT, TCT, and FECT were performed with a single test setup. The first wear test campaign, completed in 2016, included the electrical configuration characterization test (ECCT) (Ref. 16), two short duration tests (Ref. 17), and a long wear test (Ref. 17). TDU2 underwent an acceleration zone characterization test (Ref. 18) and a pole erosion characterization test (Ref. 19). TDU2 will undergo the environmental test campaign. TDU3 was used in a second performance characterization test (Ref. 20) and, together with TDU1, in a second wear test campaign (Ref. 21).

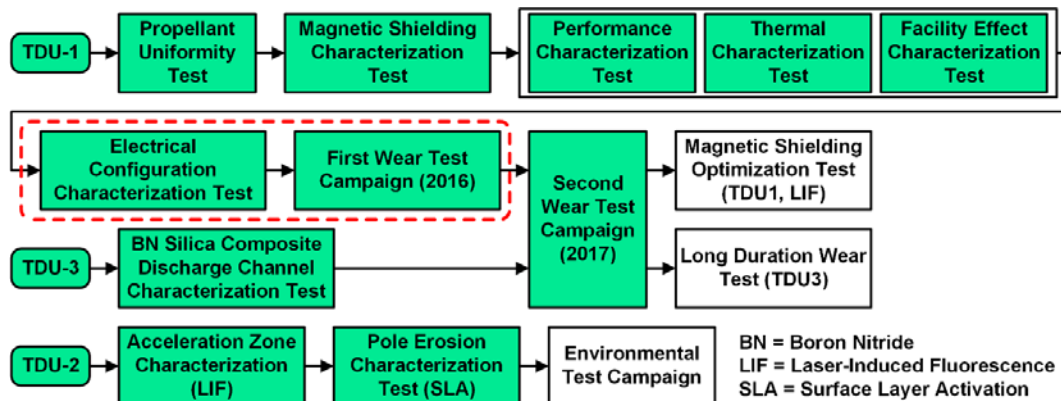


Figure 2.—A diagram of the TDU test campaign.

Additionally, Glenn Research Center (GRC) Vacuum Facility 6 (VF6) was upgraded to perform high-power electric propulsion testing. The upgrade included an enhanced version of the VF5 diagnostics system, which was used for much of the aforementioned TDU1 testing. A series of verification and validation tests, including performance, stability, and plume characterization, were performed to determine the readiness of VF6 for testing (Ref. 22). Once VF6 was determined to be operational, it was used for parts of the second wear test campaign (Ref. 21).

This paper will focus on the plasma plume characterization performed during the first wear test campaign. Specifically, this paper will begin by picking up where Peterson, et al. (Ref. 16), left off on ECCT plasma plume data analysis, then continue onto the evolution of the plasma plume characteristics over the course of the first wear test. Whereas Peterson, et al. (Ref. 16), focused more on performance and stability analysis that demonstrate the viability of cathode-tied configuration for magnetically shielded thrusters, this paper focuses more on plasma physics trends deduced from plasma plume data.

2.0 Experimental Setup

To simplify plot labeling, throttle points are labeled as vvv-kk.k, where vvv is the discharge voltage in volts and kk.k is the discharge power in kilowatts.

Unless otherwise noted, all spatial positions presented in this paper have been normalized by the mean channel diameter (MCD) of the thruster. MCD is defined as the average of the inner and outer discharge-channel wall diameters. Furthermore, thruster-centric polar axis (θ axis) is defined as 0° when viewing directly downstream from the thruster, is negative to the left of the thruster, and is positive to the right of the thruster.

2.1 Thruster and Test Matrix

All data presented in this work were collected with the HERMeS TDU1. The HERMeS TDU was designed to be a 12.5 kW, 3000 s, magnetically-shielded Hall thruster. The thruster had been operated over discharge voltages ranging from 300 to 800 V, corresponding to a specific impulse range of 2000 to 3000 s at full power. The thruster had also been power throttled over discharge powers ranging from 0.6 to 12.5 kW (Ref. 10). The cathode mass flow rate was maintained at 7 percent of the anode mass flow rate.

Thruster magnet coils were energized so that the magnetic shielding topology was always maintained. The only degree of freedom in the magnetic field setting was the strength of the magnetic field. Peak radial magnetic field strength along the discharge channel centerline was chosen as the reference when referring to the strength of the magnetic field. A single magnetic field strength value was used for all tested conditions. This value was set to provide peak thruster efficiency while maintaining margin against oscillation mode transitions. Figure 3 shows a picture of the NASA HERMeS TDU1 with various test equipment.

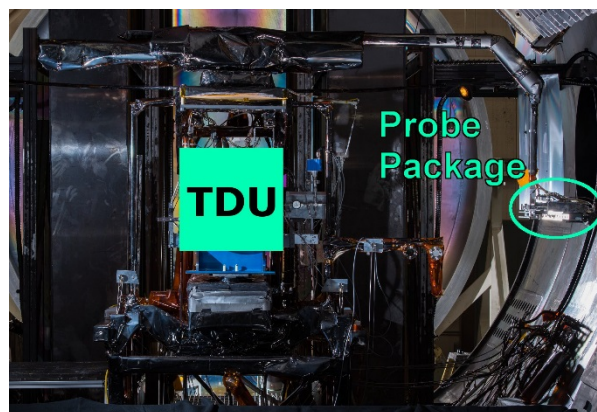


Figure 3.—NASA HERMeS TDU1 and thrust stand setup.

TABLE 1.—TABLE OF REFERENCE FIRING CONDITIONS

Label	Discharge voltage, V	Discharge power, kW
300-2.7	300	2.7
*300-6.25	300	6.25
400-8.3	400	8.33
500-10.4	500	10.4
500-12.5	500	12.5
*600-12.5	600	12.5
700-12.5	700	12.5

*RFCs that were the focus of the testing described in this paper.

TABLE 2.—A TABLE OF CONFIGURATIONS THAT CREATE A CONDUCTION PATH FOR PLASMA THROUGH THE FRONT POLES

Config → Cover mat'↓	Grounded	Floating	Cathode-tied
Graphite	Conduction path	No path	Conduction path
Alumina	No path	No path	No path

The specifications for the TDUs included seven Reference Firing Conditions (RFCs), which were throttle points that would be used in all TDU testing. Though the full operational range of the TDUs expands well beyond the RFCs, testing at all throttle points was deemed impractical and too resource intensive. Given limited time and resources, the tests described in this paper were focused on two of the RFCs. Table 1 lists the RFCs. The two RFCs that were the focus of the described tests are marked with asterisks.

During the ECCT, a total of three electrical configurations and two front pole cover materials were tested. The electrical configurations were grounded body, floating body, and body tied to cathode. The front pole cover materials were graphite and aluminum oxide (a.k.a. alumina). The pole covers were polished to provide as flat of an initial surface as possible. Note that although graphite is an electrical conductor and alumina is an electrical insulator, having graphite as the pole cover material is not the same as having a conduction path through the front poles. Specifically, in the case of graphite covers with a floating body, the front pole covers floated to a sufficiently negative voltage so that equal amounts of electrons and ions were collected by the front poles and no net current was conducted. Table 2 shows which of the six combinations of electrical configurations and pole cover materials created an electrical conduction path through the front poles. Peterson, et al., provide a more detailed description of the test setup for the ECCT (Ref. 16).

The two short wear tests were each approximately 350 hr in duration (Ref. 17). The long wear test was 996 hr in duration and was performed at the 600-12.5 RFC.

2.2 Test Facility

Testing was performed in Vacuum Facility 5 at GRC. This cylindrical facility is 4.6 m in diameter, 18.3 m long, and was evacuated with a set of cryo-panels. The thruster was mounted on a thrust stand located close to the cryo-panels, with the thruster firing away from the panels. Figure 3 shows the thruster and the plasma diagnostics, along with other test equipment in the vicinity of the thruster. Background pressure near the thruster was monitored with a set of ion gauges. Correction of gauge readings for effective sensor sensitivity was obtained by calibrating the ion gauges against a spinning rotor gauge in a controlled setup using research grade xenon. Correction of gauge readings for effects of local temperature and direction of the gauge openings relative to the background flux were obtained through a series of modeling studies and verified by experimental data (Ref. 23). Uncertainty in the calculated pressure was dominated by electrical and electronic noise, which was estimated by the manufacturer to be ± 6 percent of the reading. The background pressure near the thruster for the two RFCs described in this paper was 4.2×10^{-6} Torr.

Research-grade xenon propellant was supplied via commercially available mass flow controllers to the thruster, cathode, and auxiliary flow line. These mass flow controllers were calibrated using research-grade xenon prior to testing. Typical uncertainty of measurement was ± 1 percent of reading.

Electrical power was supplied to the thruster with commercially available power supplies. Separate power supplies supported the main discharge, cathode heater, keeper, inner magnet, and outer magnet. An electrical filter was placed between the thruster and the discharge power supply. All power supplies and the filter were located outside of the vacuum facility.

2.3 Diagnostics

This section describes the plasma diagnostics deployed during the first wear test campaign. The plasma diagnostics deployed included a Faraday probe (FP), a Langmuir probe (LP), a retarding potential analyzer (RPA), and a Wien filter spectrometer (WFS). All probes were biased with commercially available power supplies.

Figure 4 shows a photograph of the probe package and the relative position of the four probes in the package. Spatial offsets between the probes were accounted for when positioning the probes so that data from different probes can be correlated. Both the RPA and WFS were protected by independent shutters. The probe package was mounted on a boom arm, which was mounted on a set of commercially available motion stages that provided polar and radial motion. Positioning accuracy of this motion system was <1 mm for the radial axis and $<0.2^\circ$ for the polar axis. The probe package, boom arm, and the bottom of the motion stages were shielded with Grafoil to reduce the amount of backspattered material.

The FP was of GRC design (Refs. 24 and 25) and was used to measure ion current density in the far-field plume. Figure 5 shows a cross-sectional diagram of this FP. The collector and guard ring were made of molybdenum and the insulating back was made of Macor. Angular resolution of the FP data was $\sim 0.5^\circ$. At each operating condition, the FP was azimuthally swept at five different distances, 4.2, 5.2, 6.1, 7.0, and 7.9 MCD. An additional sweep at 7.9 MCD was conducted to make sure the data was not dependent on the sweep direction. During testing, measurements were made at different bias voltages in increments of 10 V. The results indicated that -30 V bias with respect to facility ground was sufficient to repel incoming electrons for all operating conditions.

The LP consisted of a single tungsten wire protruding from an alumina tube. This probe was used to obtain the local plasma potential needed to correct the RPA data. The LP was swept at 3 Hz for 1 s at each location. FP and LP data were acquired by a data acquisition device.

The RPA was of AFRL design (Refs. 24 and 25). During testing, the electron suppression and repelling grids were biased to -30 V with respect to facility ground while the ion retarding grid voltage was swept. The ion retarding grid was biased by a sourcemeter while the collected current was measured by a picoammeter. Data were taken at polar angles of $\pm 105^\circ$, $\pm 90^\circ$, $\pm 75^\circ$, $\pm 70^\circ$, $\pm 65^\circ$, $\pm 60^\circ$, $\pm 55^\circ$, $\pm 50^\circ$, $\pm 45^\circ$, $\pm 40^\circ$, $\pm 30^\circ$, $\pm 15^\circ$, and 0° . For testing with the alumina covers, additional data were taken at $\pm 85^\circ$ and $\pm 80^\circ$.

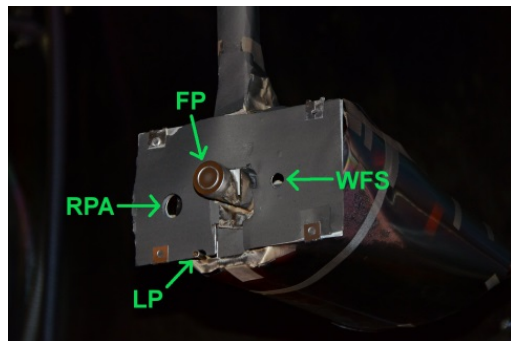


Figure 4.—The probe package.

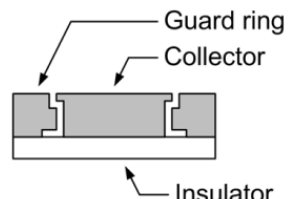


Figure 5.—Diagram of the Faraday probe.

The WFS was a commercial product and was used to measure charged species current fractions. The WFS was the product from a Small Business Innovation Research contract and has a prior history of usage (Refs. 24 to 26). The electron suppression plate was biased at -30 V with respect to facility ground to suppress secondary electron emission (SEE) from the collector. The main bias plate voltage was swept by a picoammeter, which also measured the collector current. Data was taken at 0°.

The experiment was conducted via a LabVIEW (National Instruments) program from a dedicated data acquisition computer. The computer interfaced with the motion stages via a set of motion controllers. The computer also directly interfaced with the data acquisition device, picoammeters, and sourcemeter. During the experiment, the computer automatically activated the various motion stages, shutters, and probes in the proper sequence.

3.0 Data Analysis

3.1 Faraday Probe Analysis

FP data were used to calculate the charge-weighted divergence angle and total ion beam current. The cosine of the momentum-weighted divergence angle is defined as the average axial velocity of the particles divided by the average total velocity of the particles. However, momentum-weighted divergence angle is difficult to measure. The typical approach is to measure the charge-weighted divergence angle, which is approximately equal to the momentum-weighted divergence angle if the multiply-charged current fractions are roughly constant across the interrogated domain. For the remainder of the paper, divergence angle refers to the charge-weighted divergence angle. For a polarly-swept probe, Equation (1) can be used to calculate the charge-weighted divergence angle.

$$\langle \cos \delta \rangle = \frac{2\pi R_{FP}^2 \int_0^{\pi/2} j(\theta) \cos \theta \sin \theta d\theta}{2\pi R_{FP}^2 \int_0^{\pi/2} j(\theta) \sin \theta d\theta} \quad (1)$$

Where θ is the polar angle and is equal to 0° for particles traveling parallel to the firing axis, and $j(\theta)$ is the ion current density as a function of the polar angle. R_{FP} is the distance from the Faraday probe collector to the thruster center at the exit plane and is constant for a polarly-swept probe. The denominator is equal to the total ion beam current.

A number of effects associated with the use of FP must be accounted for when performing FP analysis. To account for these effects, the FP analysis was divided into three steps. This three-step approach is a simplified version of a four-step approach validated in a previous test (Ref. 15). Whereas the four-step approach involves data from different background pressure, the three-step approach is for tests where only one background pressure was tested.

In step one, the effect of FP gap current was accounted for. For a FP with a guard ring like the one presented in this paper, the effective collection area was not exactly equal to the collector frontal surface area. Current that enters the gap between the collector and the guard ring can be collected by the side surfaces of the collector (Ref. 27). According to work by Brown, the current entering the gap is collected by the collector and the guard ring in a ratio proportional to the ratio of exposed gap area (Ref. 27). For the probe design used in the present study, the area inside the gap was dominated by guard ring surfaces (Figure 5). However, there was enough area connected to the collector that some level of correction was needed. Only the part of the gap with direct exposure to the incoming ion beam was used in the gap area calculation. Using the approach recommended by Brown, the effective collection area was ~4 percent greater than the collector frontal area. The effective collection area was used for all FP analysis.

TABLE 3.—SUMMARY OF SEE DATA FOR XENON ION BOMBARDMENT OF MOLYBDENUM (REFS. 28 AND 29)

Bombarding particle	SEE yield of molybdenum
Xe ⁺	0.022
Xe ²⁺	0.20
Xe ³⁺	0.70

In step two, the effect of SEE on FP current was corrected. Although the FP was constructed of molybdenum, which is considered a low SEE yield material, some correction for SEE effect was still needed. Secondary electrons born on a negatively biased probe will accelerate away from the probe. This effect adds extra current to the probe measurement that is indistinguishable from the collected ion current. While singly-charged xenon-induced SEE yield for molybdenum is very low (0.022) the doubly-charged xenon-induced SEE yield is roughly 10 times that of the singly-charged yield, and the triply-charged SEE yield is roughly 35 times that of the singly-charged yield (Refs. 28 to 30). Since the amount of multiply-charged species in the plume of a Hall thruster is typically not negligible, correction for SEE effect is needed.

Data published by Hagstrum was used to correct for the effect of SEE on the FP measurements. Table 3 summarizes the SEE yield values used in the data analysis of the present study. The singly-charged and doubly-charged xenon-induced yields were averages of the SEE yield data for ion energies in the range of 200 to 800 eV in Hagstrum's 1956 work on molybdenum (Ref. 29). For both of these parameters, the value measured by Hagstrum varied by no more than 10 percent of the listed average. A value for the triply-charged xenon-induced yield of molybdenum could not be found in open literature. The value in Table 3 is an extrapolated value based on the similarity in yield between tungsten and molybdenum. The ratio of triply-charged induced yield to doubly-charged induced yield for tungsten is 3.5, so the yield for molybdenum is extrapolated to be 3.5 * 0.2, or 0.7.

Equation (2) shows the relationship between the actual ion current density and the ion current density measured by the Faraday probe due to the SEE effect.

$$\frac{J}{J_{FP}} = \frac{1}{1 + \sum_k \frac{\Omega_k \gamma_k}{Z_k}} \quad (2)$$

Where J is the true ion current density, J_{FP} is the current density measured by a nude Faraday probe, and γ_k is the SEE yield in number of electrons per ion associated with bombardment by the k -th species. For the present study, the SEE correction factor varied from 0.89 to 0.95.

Hagstrum also discovered that metastable singly-charged xenon induces roughly the same SEE yield as doubly-charged xenon (Ref. 31). In that experiment, Hagstrum varied the energy of the electrons used to generate his singly-charged ion beam from 10 to 70 eV. The SEE yield measured increased from 0.022 to 0.025 when the electron energy was ramped up from 25 to 30 eV, and then plateaued at 0.025 for higher energies. While the Hall thruster ionization zone and an ion beam discharge chamber are not exactly the same, they do share many of the same operating principles, including a reliance on impact bombardment ionization. Since the amount of metastable ions was so small that the SEE yield increased by only 0.003 for Hagstrum's experiment, one can assume this effect was of similar magnitude in a Hall thruster and was negligible.

Ideally, SEE correction would have been calculated as a distribution of polar angle and applied to the FP sweeps. However, past studies have shown that variations in charged species composition with polar angle are relatively small. Data from a prior study places variation in SEE correction factor with polar angle at ~0.01 (Ref. 15). For convenience, a single SEE correction factor was applied for each operating condition.

Another factor in FP analysis is charge exchange (CEX) effect. However, not all CEX should be removed from FP data because the thruster will generate CEX ions when in space. In order to remove the influence of facility CEX without removing the signal from thruster CEX, the approach in this study was to record FP data at multiple distances.

In step three, two calculation methods were used to calculate divergence angle while removing the effect of facility CEX. In the first method, the divergence angle was calculated at each distance and plotted against distance. A linear fit was performed to determine the divergence angle at the thruster. In the second method, the current density profiles at different distances were used to extrapolate to the current density profile at the thruster, also called the “source” profile. The source profile was then used to calculate the divergence angle. The two methods yielded results that were within 0.1° of each other. From a prior study, a discrepancy of 0.1° meant the background pressure was low enough that the facility CEX effect could be corrected in the manner described here. More details about the FP analysis and how it was validated can be found in a prior publication (Ref. 15).

3.2 Langmuir Probe and Retard Potential Analyzer Analysis

LP analysis was carried out using simple Langmuir probe theory (Ref. 32). LP data were ensemble averaged then smoothed using a Savitzky-Golay filter (Refs. 33 and 34). Plasma potential was set to the probe voltage where the derivative of the probe current with respect to the probe voltage was at its maximum. This plasma potential was used to correct the RPA reading because the RPA ion retarding grid was biased with respect to the facility ground. The true filter voltage was equal to the ion retarding grid bias voltage minus the local plasma potential.

RPA analysis was carried out by first smoothing the RPA trace using a Savitzky-Golay filter, then taking the negative of the derivative of the collector current with respect to the ion retarding grid bias voltage. The result, plotted against the bias voltage, is proportional to the ion energy per charge distribution function (Ref. 35). The average ion energy per charge was calculated by averaging only the part of the trace where the amplitude exceeded half of the maximum amplitude. This averaging approach will be referred to as the threshold-based averaging approach with a 50 percent threshold. Figure 6 shows an example of applying the threshold-based averaging approach to an RPA trace. The black dashed vertical line indicates the location of the most probable voltage, the red solid vertical line indicates the result of using the threshold-based averaging approach with the 50 percent threshold, and the red dashed horizontal line indicates the 50 percent of maximum threshold.

In theory, the most accurate result would have been obtained by ensemble-averaging the entire RPA trace. However, doing so would have produced unphysical results because the ion energy per charge distribution as measured by the RPA was typically much broader than the real distribution due to the wide acceptance angle of the RPA. Using the 50 percent threshold-based averaging approach provided a balance between excluding the broadened data and maintaining noise insensitivity.

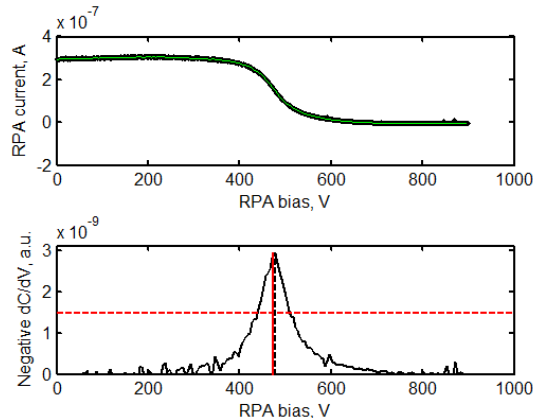


Figure 6.—Example RPA analysis plots.

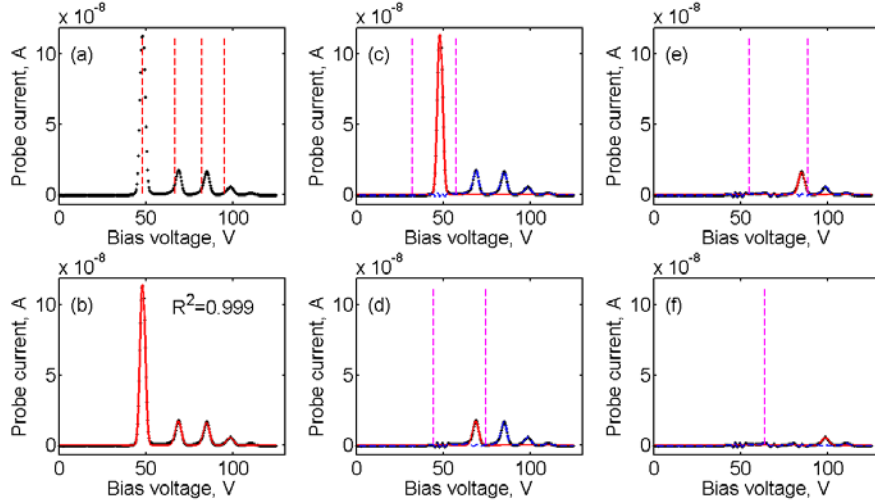


Figure 7.—Example of analysis plots for Wien filter spectrometer analysis.

3.3 WFS Analysis

The WFS was used as a velocity filter to separate charged species. Since different charged species in a Hall thruster are accelerated to different velocities, they will show up as different peaks when interrogated by the WFS. If the WFS velocity resolution is at least several times smaller than the width of the ion velocity distribution function (VDF), the preferred method for analyzing WFS data is via integration. The exact integration method used in this study was thoroughly discussed in a prior publication (Ref. 36). The curve-fit form used was the skew-normal distribution. Corrections for CEX effect were also performed in accordance to prior publications (Refs. 36 and 37).

Figure 7 shows an example of the Wien filter spectrometer analysis program results. For convenience, the subplots are labeled, top to bottom, from left to right, as (a) to (f). Subplot (a) shows the raw WFS data as black data points with red dashed vertical lines showing the approximate location of the first four peaks. Subplot (b) shows the end result from the curve-fitting process in red solid line overlaid on the raw data in black dots. Subplots (c) to (f) show the individual curve-fit steps starting from the 1st peak, then the 2nd peak, and etc. The data prior to the fit at each curve-fit sub-step are shown as black dots, the red solid line shows the curve-fit, the magenta dashed vertical lines show the curve-fit boundaries, and the blue dashed line shows the residual result after subtraction.

3.4 Uncertainty Analysis

For the calculation of the divergence angle, the primary sources of error were the axial alignment error and error induced by shift in support structure associated with facility operations. Axial alignment error was estimated to be <3 mm while shift in support structure was estimated to be <5 mm. Propagating this error through the divergence angle calculation yields an estimated error of $\pm 0.4^\circ$ for the presented data.

For the current density measurement in the FP trace, the primary sources of error on the current measurement were electronic non-linearity and noise. This error was estimated at 1 percent.

For the ion energy per charge derived from RPA measurements, uncertainty in the 50 percent threshold-based average was driven by measurement noise. This source of noise was mostly the result of plasma oscillations. The associated uncertainty was random and was characterized to be no more than ± 8 V. The Langmuir probe measurement contributed an additional 4 V of random error to the final result. Standard error propagation yielded a total random error of no more than ± 10 V.

For WFS results, the uncertainty analysis procedure described in a prior publication was used (Ref. 36). The values of the uncertainty greatly varied between RFCs with uncertainty being high for 300-6.25 and low for 600-12.5. Actual values of the uncertainties are shown in the Section 4.0.

4.0 Results

4.1 Electrical Configuration Characterization Test Plume Results and Analyses

This section begins with an examination of the ion current density, charge species fraction, and high-energy content results, in that order. Figure 8 and Figure 9 show ion current density profiles for the 300-6.25 and 600-12.5 RFCs, respectively. The differences between the six combinations of electrical configurations and pole cover materials were small with the differences at 600-12.5 being more noticeable. Specifically, there was less ion current collected between 30° and 70° for all alumina covers conditions as well as for graphite covers with floating body. Also, more current was collected at 70+° for graphite covers with floating body than for other conditions. Table 4 and Table 5 show the divergence angles calculated for each configuration for the 300-6.25 and 600-12.5 RFCs, respectively. As these two tables show, the differences in divergence angle between configurations were on the order of or less than the measurement uncertainty of $\pm 0.4^\circ$.

Figure 10 and Figure 11 show the raw WFS data for the 300-6.25 and 600-12.5 RFCs, respectively. As shown in these figures, the compositions of charged species were identical to within the uncertainty of the WFS for all tested configurations.

For the 300-6.25 RFC, the overlap between peaks were too large for the analysis program to work properly. Attempts at analysis revealed the associated uncertainty was well in excess of typical acceptable levels. No further analysis was carried out for WFS data at the 300-6.25 RFC. Table 6 summarizes the WFS analysis results for the 600-12.5 RFC in different configurations. This table shows clearly that the differences in charge species compositions between different configurations were negligible.

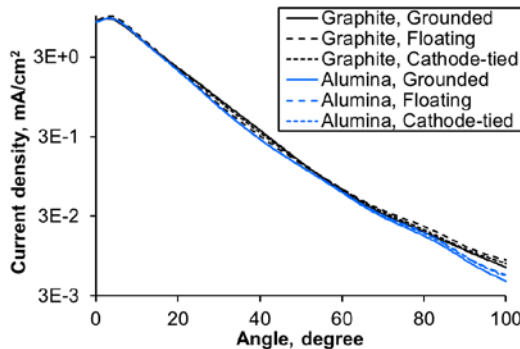


Figure 8.—Ion current density profiles for all configurations at the 300 V, 6.25 kW RFC.

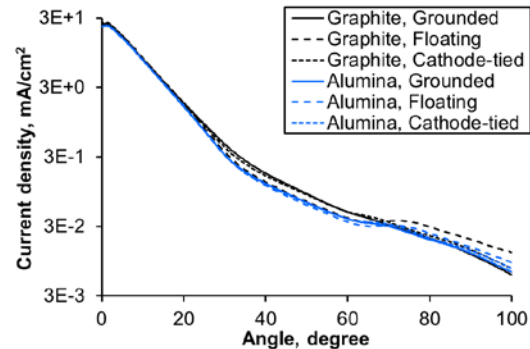


Figure 9.—Ion current density profiles for all configurations at the 600 V, 12.5 kW RFC.

TABLE 4.—DIVERGENCE ANGLE FOR THE SIX TESTED CONFIGURATIONS AT THE 300 V, 6.25 KW RFC

Config → Cover mat'↓	Grounded	Floating	Cathode-tied
Graphite	24.6°	23.9°	24.2°
Alumina	24.1°	24.2°	24.2°

TABLE 5.—DIVERGENCE ANGLE FOR THE SIX TESTED CONFIGURATIONS AT THE 600 V, 12.5 KW RFC

Config → Cover mat'↓	Grounded	Floating	Cathode-tied
Graphite	19.5°	19.4°	19.5°
Alumina	19.5°	19.8°	19.6°

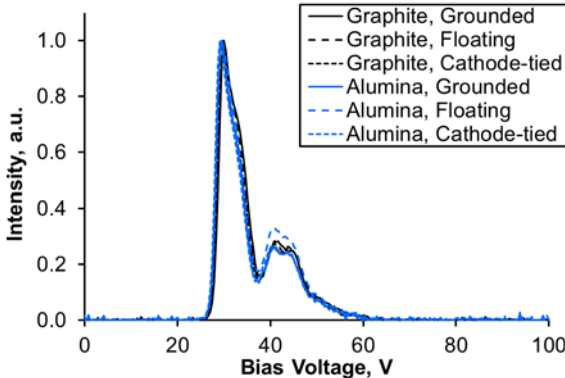


Figure 10.—Raw Wien Filter spectra for all configurations at the 300-6.25 RFC.

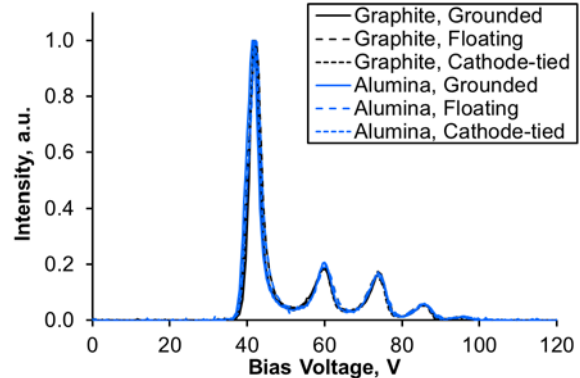


Figure 11.—Raw Wien Filter spectra for all configurations at the 600-12.5 RFC.

TABLE 6.—CHARGED SPECIES FRACTION FOR ALL CONFIGURATIONS AND AT THE 600-12.5 RFC

Config → Species ↓	Graphite, grounded	Graphite, floating	Graphite, cathode-tied	Alumina, grounded	Alumina, floating	Alumina, cathode-tied
Xe ⁺	0.83±0.02	0.86±0.02	0.85±0.02	0.87±0.02	0.86±0.02	0.86±0.01
Xe ²⁺	0.13±0.02	0.10±0.02	0.11±0.02	0.09±0.02	0.10±0.02	0.10±0.01
Xe ³⁺	0.04±0.02	0.04±0.02	0.04±0.02	0.04±0.02	0.04±0.02	0.04±0.01

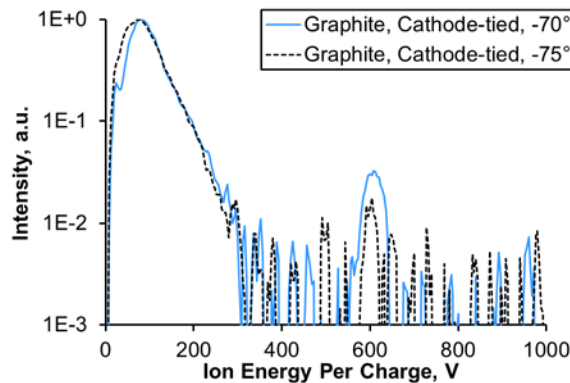


Figure 12.—Example of ion energy per charge distributions used to determine the maximum high-energy polar angle for the 600-12.5 RFC with graphite covers and cathode-tied configuration.

To examine the high-energy contents, RPA traces at many angular positions were taken. To assess the divergence of the high-energy contents, this study determined the angle at which the high-energy peak became undetectable relative to the noise floor. For example, at the 600-12.5 RFC, for the configuration with graphite covers and cathode-tied, the high-energy peak (~600 V) was detectable in the $\theta = -70^\circ$ trace but not in the $\theta = -75^\circ$ trace. The maximum high-energy polar angle was defined as the average of the two θ values with an uncertainty that spans the two θ values, which was $72.5^\circ \pm 2.5^\circ$ in this example. Negative polar angle traces were used to calculate the high-energy content properties because the RPA had a better field of view to the thruster when the probe package was on negative θ side. Figure 12 shows the two aforementioned traces of ion energy per charge. Additional visualization of the RPA data can be found in the appendix.

TABLE 7.—MAXIMUM HIGH-ENERGYPOLAR ANGLES
FOR THE 300-6.25 RFC

Config → Cover mat'l↓	Grounded	Floating	Cathode-tied
Graphite	$82.5^\circ \pm 7.5^\circ$	$82.5^\circ \pm 7.5^\circ$	$82.5^\circ \pm 7.5^\circ$
Alumina	$87.5^\circ \pm 2.5^\circ$	$87.5^\circ \pm 2.5^\circ$	$87.5^\circ \pm 2.5^\circ$

TABLE 8.—MAXIMUM HIGH-ENERGY POLAR ANGLES
FOR THE 600-12.5 RFC

Config → Cover mat'l↓	Grounded	Floating	Cathode-tied
Graphite	$82.5^\circ \pm 7.5^\circ$	$62.5^\circ \pm 2.5^\circ$	$72.5^\circ \pm 2.5^\circ$
Alumina	$62.5^\circ \pm 2.5^\circ$	$62.5^\circ \pm 2.5^\circ$	$57.5^\circ \pm 2.5^\circ$

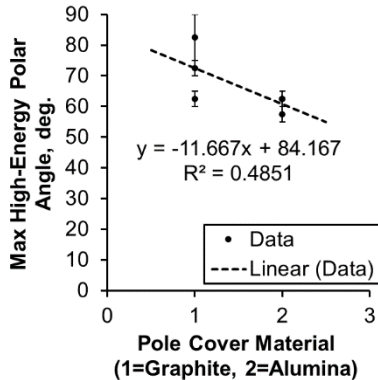


Figure 13.—Correlation analysis for max high-energy polar angle versus pole cover material for the 600-12.5 RFC.

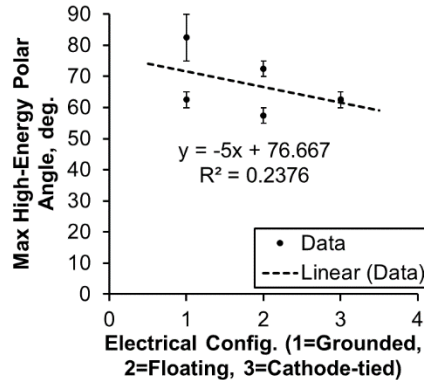


Figure 14.—Correlation analysis for max high-energy polar angle versus electrical configuration for the 600-12.5 RFC.

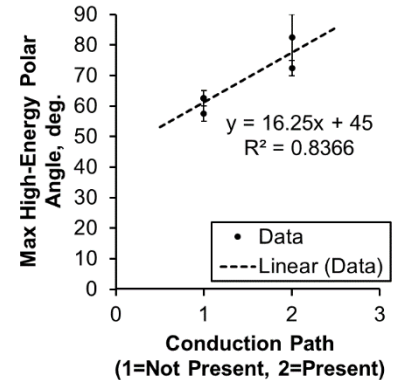


Figure 15.—Correlation analysis for max high-energy polar angle versus presence of conduction path through the front poles for the 600-12.5 RFC.

Table 7 and Table 8 summarize the maximum high-energy polar angles for the tested configurations at the 300-6.25 and 600-12.5 RFCs, respectively. Note that for Table 7, although the angles for the graphite cases appear to be smaller than the angles for the alumina cases, in reality the two sets of measurements overlap due to the large spatial uncertainty in the graphite measurements. The graphite data was measured with a coarse spatial grid ($\pm 75^\circ$ and $\pm 90^\circ$) that was refined for the alumina measurements (every 5° in the same region). Most likely, high-energy content did not appear at 90° because the outer front pole cover blocks the line-of-sight of the discharge plasma to higher polar angles. As such, the 300-6.25 data did not necessarily indicate any plasma physics trend with respect to cover material and electrical configuration. Instead, the 300-6.25 data indicated that the high-energy content reached the highest polar angle possible given line-of-sight restrictions. The presence of high-angle high-energy ions was also found in the SPT-100, which operated at 300 V (Ref. 38).

From Table 8, one can see that the high-energy content during operation with graphite covers and floating body behaved very much like the alumina covers configurations and not like the other two graphite covers configurations for the 600-12.5 RFC. Though less obvious, this trend can also be seen in the FP data in Figure 9. If one were to look at the data at polar angle less than 65° , where the high-energy content can be found, the ion current density profiles for the configurations with conduction path are slightly more divergent than the configurations without conduction path. Correlation analysis was performed to further clarify this trend. Figure 13, Figure 14, and Figure 15 show the results of correlating the maximum high-energy polar angle to pole cover material, electrical configuration, and presence of conduction path through the front poles, respectively. The R-squared value (a.k.a. coefficient of determination) indicates how much better the linear curve fit is than a simple horizontal line. An R-squared of 0 means the fit provides no predictive value while an R-squared of 1 means the fit provides perfect predictions. The correlation analysis showed clearly that the polar-angle of the high-energy

content had a much stronger correlation with the presence of a conduction path than with either the pole cover material or the electrical configuration. While more data will provide a more definitive result, the difference in R-squared values were large enough to indicate statistical significance. The divergence of the high-energy ions was driven by whether the plasma can conduct through the front poles and not by any specific pole cover material or electrical configuration.

There are at least two physical explanations for the correlation between the maximum high-energy polar angle and the presence of a conduction path through the front poles. One explanation is that when no conduction path was present, a highly negative sheath developed to repel electrons. This is supported by thruster body voltage measurements which showed the body voltage reached -45 V for graphite covers with floating body but was only 0 and -9 V for grounded and cathode-tied electrical configurations, respectively (Ref. 16). The highly negative surface voltage caused some of the high-energy ions that would normally leave the thruster to instead strike the front pole surfaces. Ions that normally leave the thruster at high polar angles were more susceptible to this effect as their trajectory brought them closer to the front pole surfaces. With these ions now striking the front pole, the overall divergence of the high-energy ions was reduced. Indeed, reducing front pole erosion by reducing the energy of ions striking the front pole was the primary motivation for developing the cathode-tied electrical configuration (Ref. 16). The data presented here suggest the possibility that reducing front pole sheath voltage also reduced the number of high-energy ions striking the front poles.

Another possibility was that the presence of the conduction path through the front poles changed (slightly) the oscillation behavior of the near-field plume. Properties of many plasma oscillation modes can be altered by changing the boundary conditions; a change in the sheath voltage on the order of tens of volts can in theory alter the magnitude of the oscillations. This possibility was supported by discharge current root-mean-squared (RMS) measurements, which were 4.0 A for graphite covers with grounded and cathode-tied configuration and 3.2 to 3.5 A for the graphite covers with floating body and for the alumina covers configurations (Ref. 16). A higher oscillation amplitude could have increased the divergence of the high-energy content without changing the number of ions striking the front poles. Periodic increases in plasma density create gradient-driven electric fields that tend to push the plasma plume radially outward. In this scenario, the disparity in maximum high-energy polar angle would have been due to the transient increase in high-energy ions at high angles as opposed to a reduction in high-energy ions striking the poles. The two explanations are associated with slightly different physical characteristics that can be investigated in a future study.

4.2 Wear Test Plume Results and Analyses

As with the ECCT results, this section will examine the ion current density, charge species fraction, and high-energy content results, in that order. Figure 16 shows the ion current density profiles measured over the course of the 996-hr wear test. Figure 17 shows the Wien Filter spectra measured over the course of the 996-hr wear test. Figure 18 and Figure 19 show the raw RPA traces measured over the course of the 996-hr wear test at $\theta = 0^\circ$ and -75° , respectively. Over the course of the long wear test, the mask in front of the RPA warped and blocked the RPA shutter from fully opening. For this reason, signal-to-noise ratio for high angle data taken at 769 and 996 hr into the test were too low and will not be shown. From these four figures, one can see that the properties of the plasma plume underwent negligible change over 996 hr of operation at the 600-12.5 RFC.

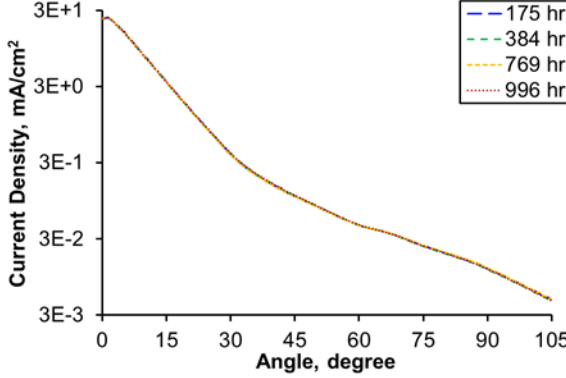


Figure 16.—Ion current density profiles measured at various points during the 996-hr wear test.

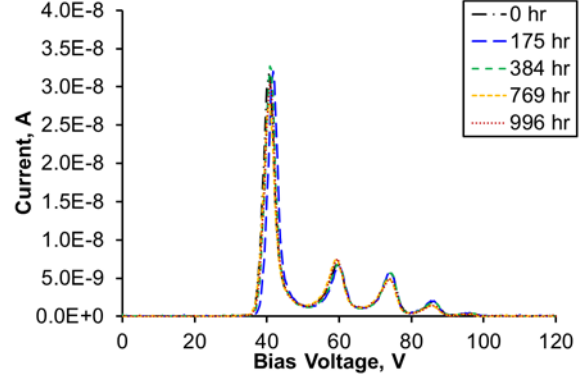


Figure 17.—Wien Filter spectra measured at various points during the 996-hr wear test.

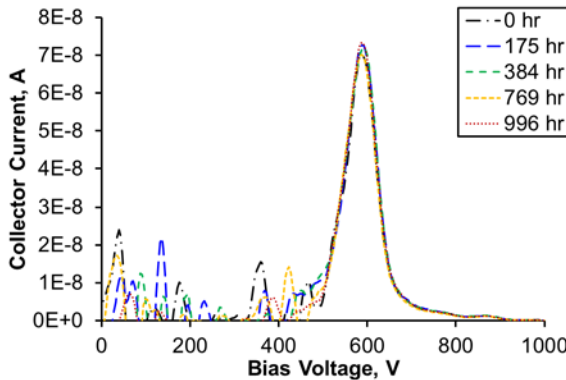


Figure 18.—Raw RPA traces at $\theta = 0^\circ$ measured at various points during the 996-hr wear test.

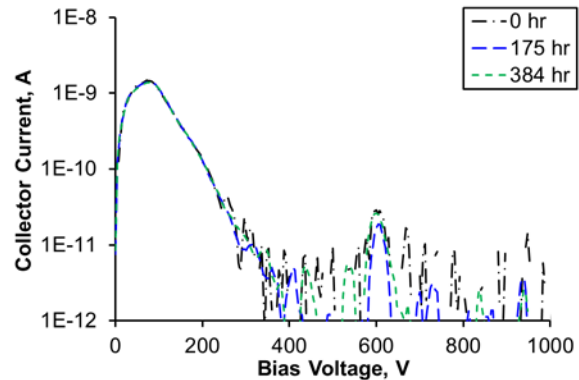


Figure 19.—Raw RPA traces at $\theta = -75^\circ$ measured at various points during the 996-hr wear test.

5.0 Conclusions

Analysis of the plasma plume characteristics during the first wear test campaign of the HERMeS TDU was completed. During the electrical configuration characterization segment of the campaign, the cathode-tied configuration was tested to ensure the thruster operated nominally while the energy of ions eroding the front poles was reduced (Ref. 16). Examination of the plasma plume data at the 300-6.25 and 600-12.5 RFCs show that the plume properties were largely unchanged across two pole cover materials (graphite and alumina) and three electrical configurations (grounded, floating, and cathode-tied). Close examination revealed that there was a noticeable difference in high-energy content behavior between graphite covers with floating body and the other two graphite covers configurations when operating at the 600-12.5 RFC. Correlation analyses revealed that the difference was driven by the presence of a conduction path through the front poles. This physical phenomenon can be explained by the possibility that reducing the magnitude of the sheath voltage by using cathode-tied configuration also reduced the number of ions striking the front poles. This physical phenomenon can also be explained by a change in plasma oscillation characteristics in the near-field plume.

Analysis of the plasma plume characteristics for the long wear test revealed that the plume underwent negligible changes over 996 hr of operation at the 600-12.5 RFC. Since the purpose of the 996-hr wear test was to uncover any unexpected failure modes, the aforementioned result was a success for this test.

Appendix—Plots of Ion Energy per Charge Distributions versus Polar Angles

Figure 20, Figure 21, Figure 22, Figure 23, Figure 24, and Figure 25 show the ion energy per charge distributions as functions of the polar angles for the six tested configurations at the 300-6.25 RFC. These plots show polar angle on the x-axis and ion energy per charge on the y-axis. Each vertical slice is an ion energy per charge distribution normalized to its peak value. Space in between slices was interpolated to provide smooth coloring for visualization purpose.

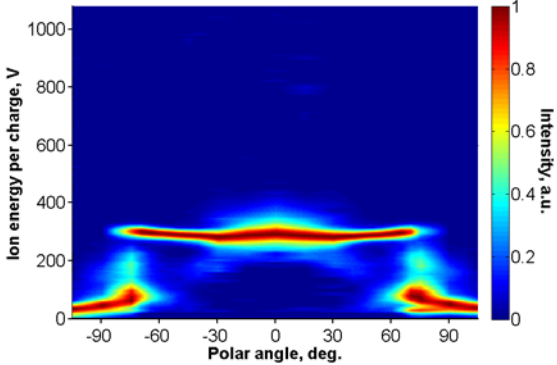


Figure 20.—Plot of ion energy per charge distribution versus polar angles for the graphite covers with grounded configuration at the 300-6.25 RFC.

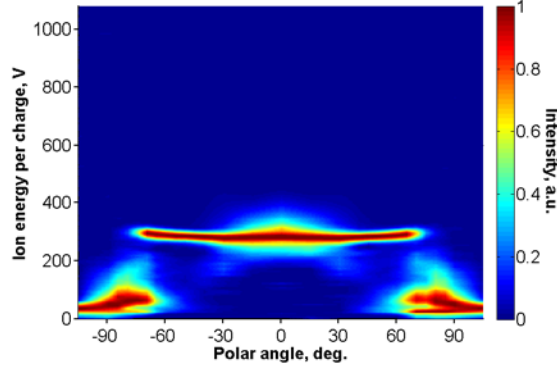


Figure 21.—Plot of ion energy per charge distribution versus polar angles for the alumina covers with grounded configuration at the 300-6.25 RFC.

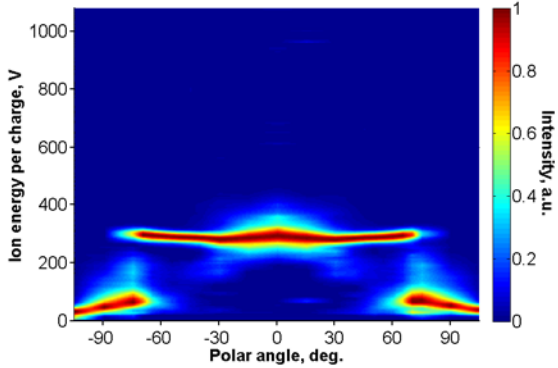


Figure 22.—Plot of ion energy per charge distribution versus polar angles for the graphite covers with floating configuration at the 300-6.25 RFC.

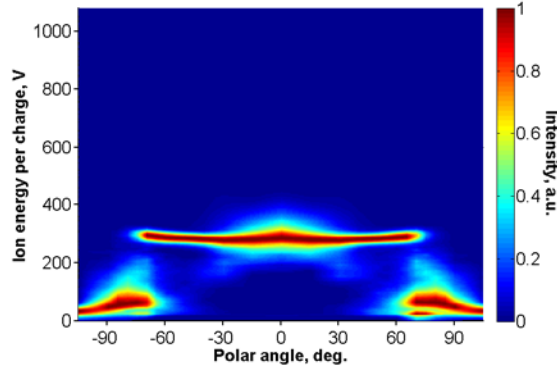


Figure 23.—Plot of ion energy per charge distribution versus polar angles for the alumina covers with floating configuration at the 300-6.25 RFC.

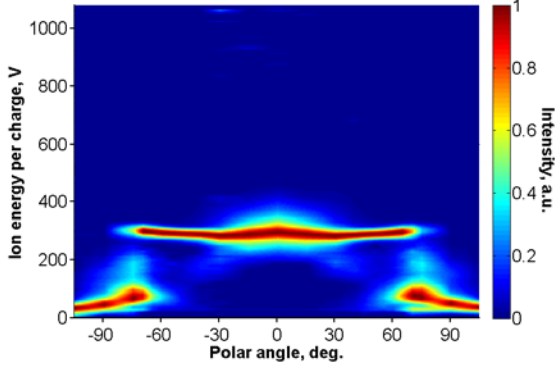


Figure 24.—Plot of ion energy per charge distribution versus polar angles for the graphite covers with cathode-tied configuration at the 300-6.25 RFC.

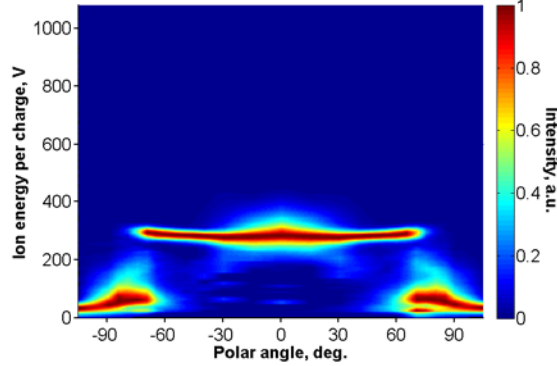


Figure 25.—Plot of ion energy per charge distribution versus polar angles for the alumina covers with cathode-tied configuration at the 300-6.25 RFC.

Figure 26, Figure 27, Figure 28, Figure 29, Figure 30, and Figure 31 show the ion energy per charge distributions as functions of the polar angles for the six tested configurations at the 600-12.5 RFC.

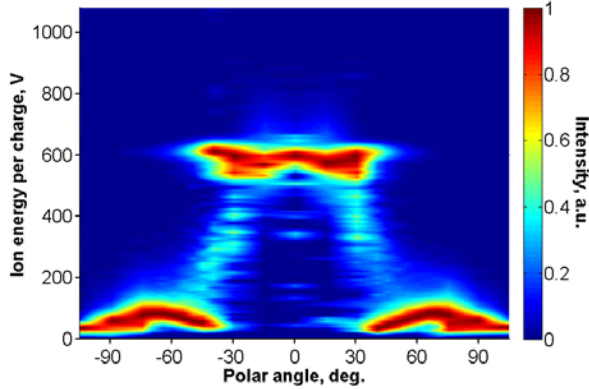


Figure 26.—Plot of ion energy per charge distribution versus polar angles for the graphite covers with grounded configuration at the 600-12.5 RFC.

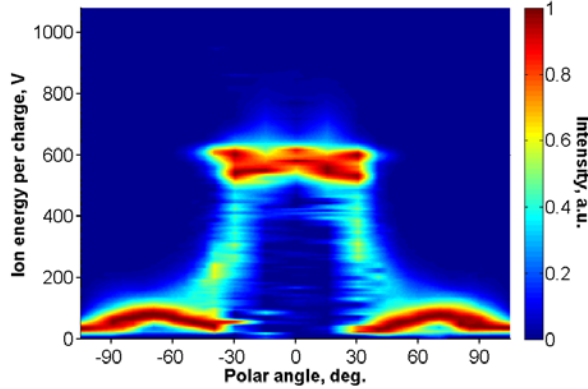


Figure 27.—Plot of ion energy per charge distribution versus polar angles for the alumina covers with grounded configuration at the 600-12.5 RFC.

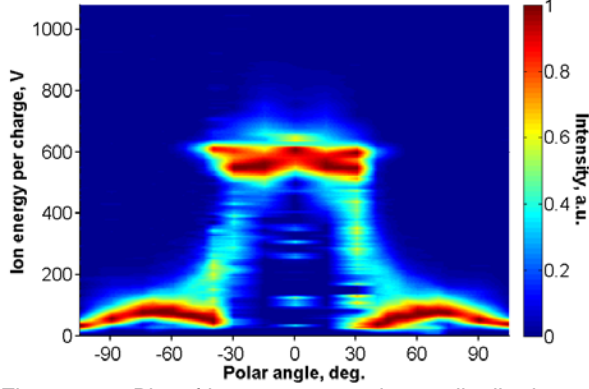


Figure 28.—Plot of ion energy per charge distribution versus polar angles for the graphite covers with floating configuration at the 600-12.5 RFC.

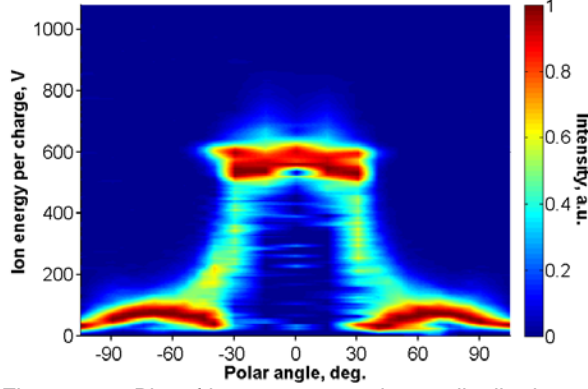


Figure 29.—Plot of ion energy per charge distribution versus polar angles for the alumina covers with floating configuration at the 600-12.5 RFC.

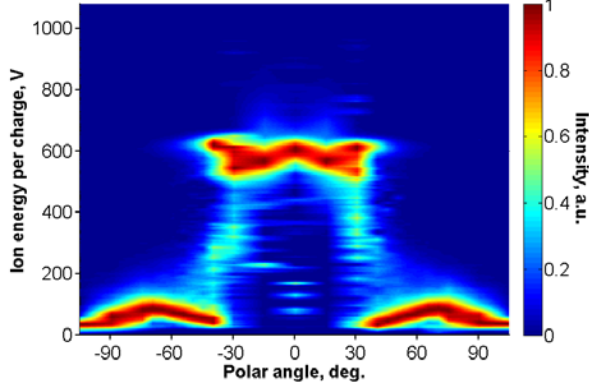


Figure 30.—Plot of ion energy per charge distribution versus polar angles for the graphite covers with cathode-tied configuration at the 600-12.5 RFC.

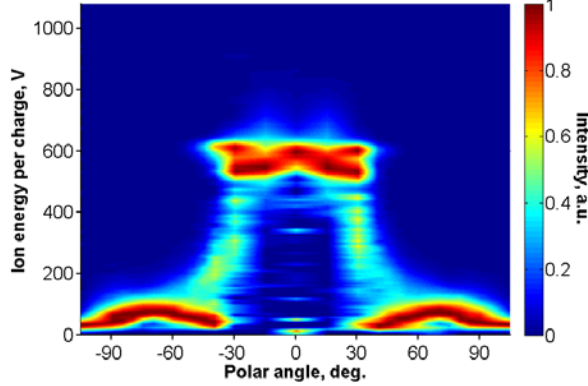


Figure 31.—Plot of ion energy per charge distribution versus polar angles for the alumina covers with cathode-tied configuration at the 600-12.5 RFC.

References

1. Smith, B.K., Nazario, M.L., and Cunningham, C.C., "Solar Electric Propulsion Vehicle Demonstration to Support Future Space Exploration Missions," Space Propulsion 2012, Bordeaux, France, May 7–10, 2012.
2. Congress, "National Aeronautics and Space Administration Transition Authorization Act of 2017," 2017.
3. NASA HQ, "Meeting Agenda and Minutes," NASA Advisory Council Human Exploration and Operations Committee Meeting, https://www.nasa.gov/sites/default/files/atoms/files/nac_heoc_march_2017_public_agenda_revb.pdf, cited: Mar 28, 2017.
4. Gerstenmaier, W., "Progress in Defining the Deep Space Gateway and Transport Plan," NASA Advisory Council Human Exploration and Operations Committee Meeting, https://www.nasa.gov/sites/default/files/atoms/files/nss_chart_v23.pdf, cited: Mar 28, 2017.
5. Manzella, D.H. and Hack, K., "High-Power Solar Electric Propulsion for Future NASA Missions," 50th AIAA/ASME/SAE/ASEE Joint Propulsion Conference, AIAA-2014-3718, doi:10.2514/6.2014-3718, Cleveland, OH, Jul 28–30, 2014.
6. Herman, D., et al., "Overview of the Development and Mission Application of the Advanced Electric Propulsion System (AEPS)," 35th International Electric Propulsion Conference, 2017-284, Atlanta, GA, Oct 8–12, 2017.
7. Hofer, R.R. and Kamhawi, H., "Development Status of a 12.5 kW Hall Thruster for the Asteroid Redirect Robotic Mission," 35th International Electric Propulsion Conference, 2017-231, Atlanta, GA, Oct 8–12, 2017.
8. Huang, W., Yim, J.T., and Kamhawi, H., "Design and Empirical Assessment of the HERMeS Hall Thruster Propellant Manifold," 62nd Joint Army-Navy-NASA-Air Force Propulsion Meeting, JANNAF-2015-3926, Nashville, TN, Jun 1–4, 2015.
9. Shastry, R., Huang, W., and Kamhawi, H., "Near-Surface Plasma Characterization of the 12.5-kW NASA TDU1 Hall Thruster," 51st AIAA/ASME/SAE/ASEE Joint Propulsion Conference, AIAA-2015-3919, doi:10.2514/6.2015-3919, Orlando, FL, Jul 27–29, 2015.
10. Kamhawi, H., et al., "Performance and Facility Background Pressure Characterization Tests of NASA's 12.5-kW Hall Effect Rocket with Magnetic Shielding Thruster," 34th International Electric Propulsion Conference, 2015-007, Kobe, Japan, Jul 4–10, 2015.
11. Huang, W., Kamhawi, H., and Haag, T.W., "Plasma Oscillation Characterization of NASA's HERMeS Hall Thruster via High Speed Imaging," 52nd AIAA/ASME/SAE/ASEE Joint Propulsion Conference, AIAA-2016-4829, doi:10.2514/6.2016-4829, Salt Lake City, UT, Jul 25–27, 2016.
12. Kamhawi, H., et al., "Performance, Facility Pressure Effects, and Stability Characterization Tests of NASA's Hall Effect Rocket with Magnetic Shielding Thruster," 52nd AIAA/ASME/SAE/ASEE Joint Propulsion Conference, AIAA-2016-4826, doi:10.2514/6.2016-4826, Salt Lake City, UT, Jul 25–27, 2016.
13. Huang, W., Kamhawi, H., Myers, J.L., Yim, J.T., and Neff, G., "Non-Contact Thermal Characterization of NASA's HERMeS Hall Thruster," 51st AIAA/ASME/SAE/ASEE Joint Propulsion Conference, AIAA-2015-3920, doi:10.2514/6.2015-3920, Orlando, FL, Jul 27–29, 2015.
14. Myers, J.L., Kamhawi, H., Yim, J.T., and Clayman, L., "Hall Thruster Thermal Modeling and Test Data Correlation," 52nd AIAA/ASME/SAE/ASEE Joint Propulsion Conference, AIAA-2016-4535, doi:10.2514/6.2016-4535, Salt Lake City, UT, Jul 25–27, 2016.
15. Huang, W., Kamhawi, H., Haag, T.W., Lopez Ortega, A., and Mikellides, I.G., "Facility Effect Characterization Test of NASA's HERMeS Hall Thruster," 52nd AIAA/ASME/SAE/ASEE Joint Propulsion Conference, AIAA-2016-4828, doi:10.2514/6.2016-4828, Salt Lake City, UT, Jul 25–27, 2016.
16. Peterson, P.Y., et al., "NASA's HERMeS Hall Thruster Electrical Configuration Characterization," 52nd AIAA/ASME/SAE/ASEE Joint Propulsion Conference, AIAA-2016-5027, doi:10.2514/6.2016-5027, Salt Lake City, UT, Jul 25–27, 2016.

17. Williams, G.J., et al., "Wear Testing of the HERMeS Thruster," 52nd AIAA/ASME/SAE/ASEE Joint Propulsion Conference, AIAA-2016-5025, doi:10.2514/6.2016-5025, Salt Lake City, UT, Jul 25–27, 2016.
18. Chaplin, V.H., et al., "Laser Induced Fluorescence Measurements of the Acceleration Zone in the 12.5 kW HERMeS Hall Thruster," 35th International Electric Propulsion Conference, 2017-229, Atlanta, GA, Oct 8–12, 2017.
19. Polk, J.E., et al., "Inner Front Pole Erosion in the 12.5 kW HERMeS Hall Thruster Over a Range of Operating Conditions," 35th International Electric Propulsion Conference, 2017-409, Atlanta, GA, Oct 8–12, 2017.
20. Kamhawi, H., et al., "Performance, Stability, and Plume Characterization Tests of the HERMeS Thruster with Boron Nitride Silica Composite Discharge Channel," 35th International Electric Propulsion Conference, 2017-392, Atlanta, GA, Oct 8–12, 2017.
21. Williams, G.J., et al., "Wear Trends of the HERMeS Thruster as a Function of Throttle Point," 35th International Electric Propulsion Conference, 2017-207, Atlanta, GA, Oct 8–12, 2017.
22. Peterson, P.Y., et al., "NASA Glenn Research Center Vacuum Facility 6 Reconfiguration for HERMeS and AEPS Programs," 35th International Electric Propulsion Conference, 2017-028, Atlanta, GA, Oct 8–12, 2017.
23. Yim, J.T. and Burt, J.M., "Characterization of Vacuum Facility Background Gas Through Simulation and Considerations for Electric Propulsion Ground Testing," 51st AIAA/ASME/SAE/ASEE Joint Propulsion Conference, AIAA-2015-3825, doi:10.2514/6.2015-3825, Orlando, FL, Jul 27–29, 2015.
24. Huang, W., Shastry, R., Soulas, G.C., and Kamhawi, H., "Farfield Plume Measurement and Analysis on the NASA-300M and NASA-300MS," 33rd International Electric Propulsion Conference, 2013-057, Washington, DC, Oct 6–10, 2013.
25. Huang, W., Kamhawi, H., and Haag, T., "Effect of Background Pressure on the Performance and Plume of the HiVHAc Hall Thruster," 33rd International Electric Propulsion Conference, 2013-058, Washington, DC, Oct 6–10, 2013.
26. Brown, D.L., "Investigation of Flow Discharge Voltage Hall Thruster Characteristics and Evaluation of Loss Mechanisms," Ph.D. Dissertation, Aerospace Engineering, University of Michigan, Ann Arbor, MI, 2009.
27. Brown, D.L. and Gallimore, A.D., "Evaluation of Facility Effects on Ion Migration in a Hall Thruster Plume," Journal of Propulsion and Power, Vol. 27, No. 3, doi:10.2514/1.B34068, May-Jun, 2011, pp. 573–585.
28. Hagstrum, H.D., "Auger Ejection of Electrons from Tungsten by Noble Gas Ions," Physical Review, Vol. 96, No. 2, doi:10.1103/PhysRev.96.325, Oct 15, 1954, pp. 325–335.
29. Hagstrum, H.D., "Auger Ejection of Electrons from Molybdenum by Noble Gas Ions," Physical Review, Vol. 104, No. 3, doi:10.1103/PhysRev.104.672, Nov 1, 1956, pp. 672–683.
30. Hagstrum, H.D., "Auger Ejection of Electrons from Tungsten by Noble Gas Ions," Physical Review, Vol. 104, No. 2, doi:10.1103/PhysRev.104.317, Oct 15, 1956, pp. 317–318.
31. Hagstrum, H.D., "Metastable Ions of the Noble Gases," Physical Review, Vol. 104, No. 2, doi:10.1103/PhysRev.104.309, Sep, 1956, pp. 309–316.
32. Lieberman, M.A. and Lichtenberg, A.J., Electrostatic Probe Diagnostics, in Principles of Plasma Discharges and Materials Processing, 2nd ed., Ch., doi:10.1002/0471724254, Wiley, New York, 2005, pp. 185–203.
33. Savitzky, A. and Golay, M.J.E., "Smoothing and Differentiation of Data by Simplified Least Squares Procedures," Analytical Chemistry, Vol. 36, No. 8, doi:10.1021/ac60214a047, Jul, 1964, pp. 1627–1639.
34. Steinier, J., Termonia, Y., and Deltour, J., "Comments on Smoothing and Differentiation of Data by Simplified Least Squares Procedure," Analytical Chemistry, Vol. 44, No. 11, doi:10.1021/ac60319a045, Sep, 1972, pp. 1906–1909.

35. Hutchinson, I.H., Principles of Plasma Diagnostics, 2nd ed., doi:10.1017/CBO9780511613630, Cambridge University Press, 2002.
36. Huang, W. and Shastry, R., “Analysis of Wien filter spectra from Hall thruster plumes,” Review of Scientific Instruments, Vol. 86, No. 7, doi:10.1063/1.4923282, Jul 6, 2015, pp. 073502.
37. Shastry, R., Hofer, R.R., Reid, B.M., and Gallimore, A.D., “Method for analyzing ExB probe spectra from Hall thruster plumes,” Review of Scientific Instruments, Vol. 80, No. 6, doi:10.1063/1.3152218, Jun 22, 2009, pp. 063502.
38. Diamant, K.D., Liang, R., and Corey, R.L., “The Effect of Background Pressure on SPT-100 Hall Thruster Performance,” 50th AIAA/ASME/SAE/ASEE Joint Propulsion Conference, AIAA-2014-3710, doi:10.2514/6.2014-3710, Cleveland, OH, Jul 28–30, 2014.

